LISA and γ-ray telescopes as multi-messenger probes of a first-order cosmological phase transition

A. Roper Pol[1,★], A. Neronov[2,3], C. Caprini[1,4], T. Boyer[2], and D. Semikoz[2]

[1] Département de Physique Théorique, Université de Genève, CH-1211 Genève, Switzerland.
[2] Université de Paris, CNRS, Astroparticule et Cosmologie, F-75006 Paris, France.
[3] Laboratory of Astrophysics, École Polytechnique Fédérale de Lausanne, CH-1015 Lausanne, Switzerland.
[4] Theoretical Physics Department, CERN, CH-1211 Genève, Switzerland.

ABSTRACT

Aims. We study two possible cosmological consequences of a first-order phase transition in the temperature range of 1 GeV to 10^3 TeV: the generation of a stochastic gravitational wave background (SGWB) within the sensitivity of the Laser Interferometer Space Antenna (LISA) and, simultaneously, primordial magnetic fields that would evolve through the Universe's history and could be compatible with the lower bound from γ-ray telescopes on intergalactic magnetic fields (IGMF) at present time.
Methods. The SGWB spectrum is evaluated adopting semi-analytical models, accounting for both the contributions from sound waves and magnetohydrodynamic (MHD) turbulence in the aftermath of the first order phase transition. Turbulence is assumed to arise only after an initial period of sound waves, and the magnetic field is assumed to be in equipartition with the turbulent kinetic energy. Several paths are considered for the magnetic field evolution throughout the radiation dominated era, in order to predict the amplitude and correlation scale of the resulting IGMF today. Comparing the SGWB level with the sensitivity of LISA and the IGMF parameters with the sensitivity reach of the CTA γ-ray telescope, we identify a range of first-order phase transition parameters providing observable signatures at both detectors.
Results. We find that, if even a small fraction of the kinetic energy in sound waves is converted into MHD turbulence, a first order phase transition occurring at temperature between 1 and 10^6 GeV can give rise to an observable SGWB signal in LISA and, at the same time, an IGMF compatible with the lower bound from the γ-ray telescope MAGIC, for all proposed evolutionary paths of the magnetic fields throughout the radiation dominated era. For two values of the fraction of energy density converted into turbulence, $\varepsilon_{\rm turb} = 0.1$ and 1, we provide the range of first-order phase transition parameters (strength α, duration β^{-1}, bubbles wall speed v_w, and temperature T_*), together with the corresponding range of magnetic field strength B and correlation length λ, that would lead to the SGWB and IGMF observable with LISA and MAGIC. The resulting magnetic field strength at recombination can also correspond to the one that has been proposed to induce baryon clumping, previously suggested as a possible way to ease the Hubble tension. In the limiting case $\varepsilon_{\rm turb} \ll 1$, the SGWB is only sourced by sound waves, however, an IGMF is still generated. We find that values as small as $\varepsilon_{\rm turb} \sim \mathcal{O}(10^{-13})$ (helical) and $\mathcal{O}(10^{-9})$ (non-helical) can provide IGMF compatible with MAGIC's lower bound.

Key words. gravitational waves – magnetic fields – cosmology: early Universe – magnetohydrodynamics – cosmology: observations – cosmology: cosmic background radiation

1. Introduction

Magnetic fields are ubiquitous at all scales in the Universe. In particular, observations from TeV blazars suggest the existence of intergalactic magnetic fields (IGMF) in the cosmic voids of the Large Scale Structure (LSS) with a lower bound in their strength of $B > 1.8 \times 10^{-17}$ Gauss at scales $\lambda_B \gtrsim 0.2$ Mpc (Neronov & Vovk 2010; Acciari et al. 2023). Although the origin of these IGMF is still unclear, a seed of cosmological origin might be the most plausible explanation, since astrophysical mechanisms (e.g., via Biermann battery) seem to lack the potential to generate IGMF in cosmic voids with a large volume filling factor (Dolag et al. 2011).

The presence of a primordial magnetic field in the early Universe is, on the other hand, constrained by the Big Bang Nucleosynthesis (BBN) limit (first analyzed in Shvartsman (1969)) as well as by the Cosmic Microwave Background (CMB) experiments (Ade et al. 2016; Galli et al. 2022). Several mechanisms have been proposed that would lead to the generation of magnetic fields from cosmological phase transitions, especially if the phase transition is of first order; see Durrer & Neronov (2013) and Vachaspati (2021) for reviews and references therein. According to the Standard Model (SM), both the electroweak and the Quantum Chromodynamics (QCD) transitions have occurred as crossovers in the early Universe (Kajantie et al. 1996; Stephanov 2006). However, extensions of the SM can provide the required conditions for baryogenesis at the electroweak scale and

---

★ corresponding author [e-mail: `alberto.roperpol@unige.ch`]

would produce, at the same time, a first-order phase transition; see Caprini et al. (2020) for a review.

First-order phase transitions, as well as turbulent motion, around the electroweak scale, can be responsible for the production of a stochastic gravitational wave background (SGWB) (see, e.g., Kamionkowski et al. (1994)) detectable by the Laser Interferometer Space Antenna (LISA) (Amaro-Seoane et al. 2017). Due to the high conductivity in the early Universe, a magnetic field would interact with the primordial plasma, inevitably leading to the development of magnetohydrdynamic (MHD) turbulence (Brandenburg et al. 1996). The production of GWs from (M)HD turbulence has been extensively studied (see Caprini & Figueroa (2018) for a review and references therein) and, recently, numerical simulations (Roper Pol et al. 2020) have provided the tools to compute and validate an analytical template for the SGWB (Roper Pol et al. 2022a).

Primordial magnetic fields generated at a phase transition have a characteristic length scale that is limited by the size of the horizon, e.g., $\tilde{\lambda}_H \sim 10^{-9}$ Mpc (redshifted to present time due to the expansion of the Universe) for a temperature scale $T_* \sim 100$ GeV. The magnetic field follows a dynamical evolution driven by decaying turbulence from the time of its generation until the end of the radiation-dominated era. Later on, the characteristic turbulent power-law evolution of the magnetic field strength and length scale become logarithmic functions of the cosmic time, such that the field evolution at large scales is virtually frozen (Banerjee & Jedamzik 2004; Subramanian 2016).

The details of the field evolution during the radiation-dominated era are not fully understood. If the turbulent decay of non-helical magnetic fields from the electroweak epoch proceeds through the "selective decay" of short-range modes (Banerjee & Jedamzik 2004), its present day relic strength is expected to be below the lower bound from the γ-ray observations, when the redshifted size of the horizon is around 10^{-9} Mpc or smaller (for $T_* \gtrsim 100$ GeV) and the comoving initial field strength is limited by the BBN bound $\tilde{B} \lesssim 10^{-6}$ G (Kahniashvili et al. 2011). On the contrary, helicity-conserving decay of helical magnetic fields leads to an inverse cascade that amplifies the magnetic field length scale and the field amplitude at large scales, while the magnetic energy density decays (Banerjee & Jedamzik 2004). Hence, helical fields are compatible with the IGMF inferred from the γ-ray observations for a larger set of initial conditions. However, it has been argued from simulations that a similar large scale field amplification can also occur for non-helical fields (Brandenburg et al. 2015). This has later been derived also using theoretical arguments: Hosking & Schekochihin (2022) propose that the conservation of local helicity fluctuations, characterized by the so-called Hosking integral (Zhou et al. 2022), can lead to an inverse cascade even when the net helicity is zero. Therefore, fields produced around the electroweak scale with *any* fractional helicity could, in principle, provide a seed field compatible with the γ-ray lower bounds on the IGMF.

In addition, Jedamzik & Pogosian (2020) proposed that a primordial magnetic field present at recombination, with sufficient amplitude, could reduce the sound horizon by inducing baryon clumping, which would affect the estimate of the present-time Hubble constant from CMB data in a way that would relax the "Hubble tension". Neronov et al. (2021) and Roper Pol et al. (2022a) showed that a non-

helical field originated at the QCD phase transition could satisfy the γ-ray lower bound on the IGMF, induce enough baryon clumping (Jedamzik & Pogosian 2020; Galli et al. 2022), and generate the SGWB that has been recently detected by several pulsar timing array collaborations (Agazie et al. 2023; Antoniadis et al. 2023a; Reardon et al. 2023; Xu et al. 2023) (see in particular Antoniadis et al. (2023b), where (M)HD turbulence was analyzed as a possible source of the SGWB, and Afzal et al. (2023), where instead sound waves and bubble collisions were analyzed).

In the present work, we provide a framework to study a first order phase transition with a "multi-messenger" approach. On one hand, we analyze the detectability by LISA of a SGWB produced around the electroweak scale, from both sound waves (Hindmarsh et al. 2014) and (M)HD turbulence. On the other hand, we analyze the evolution down to recombination of a magnetic field also generated around the electroweak scale, compatible with the aforementioned SGWB, and determine whether it can explain the blazars' observations in the cosmic voids of the LSS, the CMB and BBN constraints, as well as the possibility that it can alleviate the Hubble tension.

In the following, the notation is such that all characteristic scales and time intervals are physical, and therefore time dependent. They are understood to be redshifted when compared with quantities at the present time, e.g., with the GW frequency f or with the conformal Hubble factor at the phase transition time, $\mathcal{H}_* \equiv (a_*/a_0)\, H_*$.

2. Models for the stochastic gravitational wave background

We study the potential detectability of a SGWB from a first-order phase transition around the electroweak scale, incorporating updated results on the contributions to the SGWB from sound waves (Hindmarsh & Hijazi 2019; Jinno et al. 2023) and (M)HD turbulence (Roper Pol et al. 2022a). Since it has been found that the electroweak phase transition bubbles hardly run away (Bodeker & Moore 2017), we ignore the contribution to the SGWB from broken-phase bubble collisions.

Following Caprini et al. (2016, 2020), we characterize the phase transition by four parameters:

1. T_* is the phase transition temperature (interpreted as the percolation temperature for a weak to moderately strong thermal phase transition).
2. β is the rate of change of the nucleation rate of the broken-phase bubbles. Its inverse value at the moment of the phase transition can be considered as a characteristic time scale of the phase transition, $t_\beta = \beta^{-1} \lesssim H_*^{-1}$, where H_* is the expansion rate at the epoch of the phase transition.
3. α characterizes the strength of the phase transition: it represents the vacuum energy density in the symmetric phase released in the broken-phase bubbles, in units of the radiation energy density,[1] $\alpha = \rho_{\text{vac}}/\rho_{\text{rad}}^*$.
4. v_w is the velocity of the broken-phase bubbles.

---

[1] Note that this parameter has also been generalized beyond the bag equation of state using, for example, the trace anomaly of the energy momentum tensor or the difference among the energies in the two phases (Caprini et al. 2020). In practice, for the purpose of this work, all three definitions would be equivalent.

Apart from these dynamical parameters, the inclusion of (M)HD turbulence in the calculation of the SGWB spectrum adds another parameter:

5. $\varepsilon_{\rm turb}$ is the fraction of the kinetic energy density induced in the primordial plasma by the bubble expansion and collision that is converted from sound waves into vortical turbulent motions.

In the analysis of possible SGWB spectra from a cosmological first-order phase transition, we scan the four-dimensional parameter space $(T_*, \beta, \alpha, v_w)$ and consider two possible levels of $\varepsilon_{\rm turb} = 0.1$ and 1.

The resulting SGWB spectrum is the addition of two contributions: sound waves and (M)HD turbulent plasma motions. The interplay between these two contributions is uncertain and it is an open, active topic of research. In this work, we assume that sound waves (compressional motions) produce GWs from the time of bubble collision until the development of non-linearities at $t_{\rm nl} \sim \lambda_*/\sqrt{K}$, where K is the kinetic energy density fraction and λ_* is the characteristic length scale of the fluid motion; see Sec. 2.1. After this time, vortical (M)HD turbulence is produced as a consequence of the development of non-linearities from the initial sound waves, yielding an additional contribution to the SGWB, and the remaining compressional motion is assumed to have dissipated. We assume that the turbulent sourcing of GWs operates only in the decaying phase, which amounts to assuming that the development of turbulence is instantaneous. Since the details of the turbulence generation from the non-linearities and shocks after the sound wave dominated phase are unknown, we remove this potential source of uncertainties in the determination of the resulting SGWB (Roper Pol et al. 2020, 2022b; Brandenburg et al. 2021; Roper Pol et al. 2022a).

Alternatively, both compressional and vortical motions (i.e., the development of turbulence) could occur directly together at the time of bubble collisions. In this scenario, the energy density of each contribution would directly come from the energy budget available from the first-order phase transition (for example, a fraction γ of the total kinetic energy transferred to the fluid by the bubble expansion would go into compressional or acoustic modes, and a fraction $1 - \gamma$ into vortical modes). The limiting case $\gamma = 0$, corresponding to only turbulence being produced at the phase transition, was considered in Roper Pol et al. (2022a). We compare the results of our analysis, in which we always account for the initial compressional phase characterized by sound waves, with the results of Roper Pol et al. (2022a) in Sec. 3.

For the sound wave component, we consider two templates. The first one is based on the sound shell model (SSM) of Hindmarsh (2018) and Hindmarsh & Hijazi (2019), including the correction for short shock times (Caprini et al. 2020). In this model, the spectrum has two breaks, one at the frequency corresponding to the inverse mean size of the broken-phase bubbles, λ_*^{-1}, and one at the scale corresponding to the inverse sound shell thickness, $\delta\lambda_*^{-1} \geq \lambda_*^{-1}$. In order to ensure the correct hierarchy of scales proposed within the SSM, we fix $v_w > 0.3$, since lower v_w would yield $\delta\lambda_*^{-1} \leq \lambda_*^{-1}$. The spectral shape is a double broken power law, proportional to f^9 at small $f \lesssim \lambda_*^{-1}$, proportional to f at intermediate $\lambda_*^{-1} \lesssim f \lesssim \delta\lambda_*^{-1}$, and proportional to f^{-4} at large f. Since we rely on analytical templates, in this work we do not account for the fact

that the SSM shape, in particular the intermediate slope, likely has a more complicated dependence on v_w, as shown in Gowling & Hindmarsh (2021).

The f^9 part of the spectrum based on the SSM of Hindmarsh & Hijazi (2019) does not seem to agree with the recent numerical studies of Jinno et al. (2023) using the so-called Higgsless (HL) simulations, as well as with the analytical analysis of Cai et al. (2023). Hence, we consider a second template based on the results of the HL simulations. In this case, a spectrum proportional to f^3 is found at small frequencies, with f and f^{-3} scaling at intermediate and large f, respectively. The behavior at large frequencies is actually not in contradiction with that of Hindmarsh & Hijazi (2019) since their fit asymptotically tends to f^{-4} but their numerical results show a f^{-3} spectrum, being their fit accurate at small and moderate f. The difference between the two templates, which are described in Sec. 2.1, is illustrated in Fig. 1.

The SGWB from the turbulent component is described in Sec. 2.2. It is based on the model presented and validated with simulations of MHD turbulence in Roper Pol et al. (2022a). This model has also been validated for purely kinetic turbulence in Auclair et al. (2022). Even though this model applies to non-helical fields, the numerical simulations in Roper Pol et al. (2022b) indicate that the resulting SGWB for decaying turbulence does not significantly depend on the fractional helicity. Therefore, we apply our findings to the case of helical magnetic fields as well, in particular when we consider the time evolution of the field (cf. Fig. 4).

The turbulent spectrum as well presents two breaks. In this case, the first break corresponds to the inverse effective duration of the turbulence, $\delta t_{\rm fin}^{-1}$, and the second one is $f_{\rm turb} \sim \mathcal{O}(\lambda_*^{-1})$. The first break in the GW spectrum is from f^3 to f, and the second break (the peak of the spectrum) is from f to $f^{-8/3}$ if one assumes Kolmogorov turbulence in the initial conditions. Note that this template applies under the assumption that turbulence is generated instantaneously. The resulting sound wave and turbulence templates are shown in Fig. 1 for a specific choice of the parameters describing the phase transition.

## 2.1. Gravitational wave background from sound waves

The template of the spectrum of GWs from sound waves relies on the updated analysis of Hindmarsh & Hijazi (2019), in the framework of the SSM (Hindmarsh 2018). Within this model, the GW power spectrum has two characteristic scales. The first one is the mean size of the broken-phase bubbles at the moment of percolation,

$$\lambda_* = \frac{(8\pi)^{1/3} \max(v_w, c_{\rm s})}{\beta}, \qquad (1)$$

where $c_{\rm s}$ is the sound speed, taken to be $c_{\rm s} = 1/\sqrt{3}$ during the radiation-dominated era. We have added the correction at low v_w, following Caprini et al. (2020) and Ellis et al. (2020). The second scale is the sound shell thickness (Hindmarsh & Hijazi 2019),

$$\delta\lambda_* = \Delta_w \lambda_*, \quad \text{with} \quad \Delta_w = \frac{|v_w - c_{\rm s}|}{v_w}. \qquad (2)$$

We adopt the following analytic expression to approximate the SSM SGWB spectrum (Hindmarsh & Hijazi 2019; Hind-
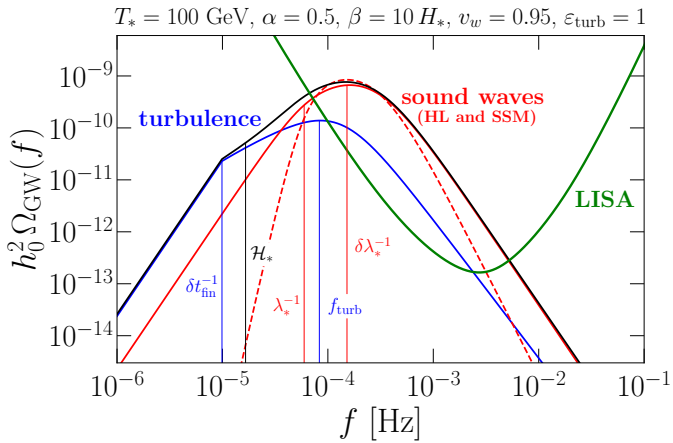
Fig. 1. Spectra of the different components of the SGWB for $T_* = 100$ GeV, $\alpha = 0.5$, $\beta = 10H_*$, $v_w = 0.95$, and $\varepsilon_{\text{turb}} = 1$, compared to LISA's power law sensitivity from Caprini et al. (2020) with a signal-to-noise ratio threshold of 10. The SGWB spectra from sound waves are based on the SSM of Hindmarsh & Hijazi (2019) (dashed red) and on the fit from HL simulations of Jinno et al. (2023) (solid red). The spectrum of the turbulence is based on the model developed in Roper Pol et al. (2022a). The vertical lines indicate the relevant frequencies of the turbulence template ($\delta t_{\text{fin}}^{-1}$ and f_{turb}) in blue, of the sound wave template (λ_*^{-1} and $\delta\lambda_*^{-1}$) in red, and the conformal Hubble frequency $\mathcal{H}_*$ at the time of GW generation in black.

marsh et al. 2021):

$$\Omega_{\text{GW}}^{\text{sw}}(f) = 3\,\mathcal{B}(\Delta_w)\frac{(K\lambda_*\mathcal{H}_*)^2}{\sqrt{K}+\lambda_*\mathcal{H}_*}F_{\text{GW}}^0\,S_{\text{sw}}(s_1, s_2, \Delta_w), \quad (3)$$

where S_{sw} is the spectral shape, given in Eq. (6) for the SSM and in Eq. (7) for the fit based on HL simulations. $s_1 = \lambda_* f$ and $s_2 = \delta\lambda_* f$ are the frequencies expressed in units of each of the relevant scales. The GW efficiency is $\mathcal{B} = \tilde{\Omega}_{\text{gw}}/\mu(\Delta_w)$, where $\tilde{\Omega}_{\text{gw}} \sim \mathcal{O}(10^{-2})$ is the integrated value of the spectrum, based on numerical simulations (Hindmarsh et al. 2017). The normalization variable μ is defined to ensure that the integral of S_{sw}/μ over $\ln f$ is unity. It is a function of the sound-shell thickness,

$$\mu(\Delta_w) = \int_0^\infty S_{\text{sw}}(f, \lambda_*, \Delta_w)\,\mathrm{d}\ln f. \quad (4)$$

K denotes the amount of sound wave kinetic energy density as a fraction of the total energy density:

$$K = \frac{\rho_{\text{K}}}{\rho_{\text{vac}} + \rho_{\text{rad}}^*} = \frac{\kappa_v\alpha}{1+\alpha}, \quad (5)$$

where $\kappa_v \equiv \rho_{\text{K}}/\rho_{\text{vac}}$ is the fraction of the vacuum energy released that is converted to kinetic energy density of the plasma ρ_{K} (Espinosa et al. 2010). Therefore, in (5) we make the implicit assumption that the totality of the kinetic energy available from the phase transition is in the form of sound waves. In the simulations of Hindmarsh et al. (2017), it has been demonstrated that this is a good assumption for small α. We use the results of Espinosa et al. (2010) to calculate κ_v as a function of α and v_w.

The spectral shape S_{sw} in the SSM is a function of the frequency s_2, expressed in units of the global peak frequency $\delta\lambda_*^{-1}$, and the sound shell thickness,

$$S_{\text{sw}}^{\text{SSM}}(s_2, \Delta_w) = s_2^9\left(\frac{\Delta_w^4+1}{\Delta_w^4+s_2^4}\right)^2\left(\frac{5}{5-m+ms_2^2}\right)^{\frac{5}{2}}, \quad (6)$$

where $m = (9\Delta_w^4 + 1)/(\Delta_w^4 + 1)$, such that $S_{\text{sw}}^{\text{SSM}} = 1$ at the peak $s_2 = 1$.

On the other hand, following Jinno et al. (2023), we also consider a double broken power law with slopes 3, 1, and -1 at small, intermediate, and large frequencies, respectively, expressed again in terms of the frequencies s_1 and s_2,

$$S_{\text{sw}}^{\text{HL}}(s_1, s_2, \Delta_w) = \frac{16\,(1+\Delta_w^{-3})^{\frac{2}{3}}(\Delta w\,s_1)^3}{(1+s_1^3)^{\frac{2}{3}}(3+s_2^2)^2}. \quad (7)$$

Hence, the spectral shape of this fit is based on the results of the HL simulations of Jinno et al. (2023), while the frequency breaks and the amplitude are taken from the SSM. The spectral shape is normalized such that $S_{\text{sw}}^{\text{HL}} = 1$ at the peak $s_2 = 1$.

Finally, the transfer function F_{GW}^0 that takes into account the redshift of the GW energy density is

$$F_{\text{GW}}^0 = \left(\frac{a_*}{a_0}\right)^4\left(\frac{H_*}{H_0}\right)^2 \simeq 1.64\,h_0^{-2} \times 10^{-5}\left(\frac{100}{g_*}\right)^{\frac{1}{3}}, \quad (8)$$

where $h_0 = H_0/(100$ km/s/Mpc$)$.

2.2. Gravitational wave background from (M)HD turbulence

To model the production of GWs from (M)HD vortical turbulence, we follow the results presented in Roper Pol et al. (2022a): we assume that the turbulence onset is instantaneous and that, afterwards, the GW sourcing stresses are constant in time during the GW production, i.e., for a time that we denote δt_{fin} (more detail about this quantity is given below). This assumption gives a good approximation to the SGWB signal evaluated by numerical simulations in which the turbulence is inserted in the initial conditions, as demonstrated in Roper Pol et al. (2022a) for MHD turbulence and in Auclair et al. (2022) for purely vortical kinetic turbulence. The SGWB spectrum reads:

$$\Omega_{\text{GW}}^{\text{turb}}(f) = 3\,\mathcal{A}\,\Omega_*^2\,(\lambda_*\mathcal{H}_*)^2 F_{\text{GW}}^0\,S_{\text{turb}}(s_1, s_3). \quad (9)$$

The amplitude of the SGWB spectrum scales with the square of the fraction of the total turbulent energy density Ω_*, given by the sum of the vortical velocity component and the magnetic field. We assume Ω_* to be a fraction $\varepsilon_{\text{turb}}$ of K,

$$\Omega_* = \Omega_{B*} + \Omega_{v*}^\perp = \frac{\rho_{B*} + \rho_{v*}^\perp}{\rho_{\text{vac}} + \rho_{\text{rad}}^*} = \varepsilon_{\text{turb}}K, \quad (10)$$

where ρ_{B*} is the magnetic energy density, $\rho_{v*}^\perp$ is the vortical component of the kinetic energy density, and Ω_{B*} and $\Omega_{v*}^\perp$ are their ratios to the total energy density. Note that $\Omega_{v*}^\perp$ refers to kinetic vortical motions while K, defined in Eq. (5), refers to the kinetic compressional motions in the form of sound waves.

Following Banerjee & Jedamzik (2004), we assume that the fields are in equipartition, so that $\Omega_{v*}^\perp \simeq \Omega_{B*} \simeq \frac{1}{2}\Omega_*$. We define the characteristic velocity u_* to be the maximum of the enthalpy-weighted rms fluid velocity v_f and the Alfvén speed v_A. For a radiation-dominated Universe with pressure $p = c_s^2\rho_{\text{rad}} = \frac{1}{3}\rho_{\text{rad}}$ and subrelativistic bulk motions, v_A is (Brandenburg et al. 1996)

$$v_A^2 = \frac{\langle B^2\rangle}{\langle\rho_{\text{rad}}+p\rangle} = \frac{2\,\Omega_B}{(1+c_s^2)} = \frac{3}{2}\Omega_B, \quad (11)$$

and v_f, considering only vortical motion $v_\perp$, is

$$v_f^2 = \frac{\langle \rho v_\perp^2 \rangle}{\langle \rho_{\rm rad} + p \rangle} = \frac{2\,\Omega_v^\perp}{(1 + c_s^2)} = \frac{3}{2}\Omega_v^\perp. \tag{12}$$

From Eqs. (11) and (12), we find that the characteristic velocity u_*, assuming equipartition, is

$$u_* = \sqrt{\frac{3}{2}\max(\Omega_{v*}^\perp, \Omega_{B*})} \simeq \sqrt{\frac{3}{4}\Omega_*}. \tag{13}$$

The parameter $\delta t_{\rm fin}$ represents the effective turbulence duration, and we express it in terms of a multiple of the eddy turnover time, $\delta t_{\rm fin} = \mathcal{N}\lambda_*/u_*$. According to the numerical simulations in Roper Pol et al. (2022a), one can set $\mathcal{N} \simeq 2$. Note, however, that the value of $\mathcal{N}$ is a subject of ongoing study. The effective turbulence duration determines the position of the first break in the SGWB spectrum, occurring at $f \sim \delta t_{\rm fin}^{-1}$.

The SGWB spectral shape in Eq. (9) is given by $S_{\rm turb}(s_1, s_3)$, where $s_3 = \delta t_{\rm fin} f$ denotes the frequency in units of the inverse effective duration of the turbulence. We recall that $s_1 = \lambda_* f$: as usual, we assume that the initial correlation length of the turbulence corresponds to the mean size of the broken-phase bubbles at the onset of their collisions, λ_*, given in Eq. (1). This determines the position of the global peak of the spectrum, located at $s_{\rm turb} \equiv \lambda_* f_{\rm turb} \gtrsim 1$. The exact value of $s_{\rm turb}$ depends on the spectral shape of the anisotropic stresses $p_\Pi(s_1)$, see Eqs. (17)–(20).

The spectral shape $S_{\rm turb}$ is determined both by the anisotropic stress power spectrum itself, and by how the latter sources the GWs in time. Assuming that the sourcing process is constant in time over the duration $\delta t_{\rm fin}$ provides the following SGWB spectral shape:

$$S_{\rm turb}(s_1, s_3) = \frac{4\pi^2 \, s_1^3 \, \mathcal{T}_{\rm GW}(s_1, s_3)}{(\lambda_* \mathcal{H}_*)^2} \frac{p_\Pi(s_1)}{s_{\rm turb}\, p_\Pi(s_{\rm turb})}, \tag{14}$$

with $\mathcal{T}_{\rm GW}$ being (Roper Pol et al. 2022a),

$$\mathcal{T}_{\rm GW}(s_1, s_3) = \begin{cases} \ln^2\!\big[1 + \mathcal{H}_*\delta t_{\rm fin}/(2\pi)\big], & \text{if } s_3 < 1, \\ \ln^2\!\big[1 + \lambda_* \mathcal{H}_*/(2\pi s_1)\big], & \text{if } s_3 \geq 1. \end{cases} \tag{15}$$

$S_{\rm turb}$ is normalized such that its maximum is approximately one. Its exact value at the peak $f_{\rm turb}$, where $s_3 = \delta t_{\rm fin} f_{\rm turb} > 1$, is

$$S_{\rm turb}(s_{\rm turb}) = 4\pi^2 \left(\frac{s_{\rm turb}}{\lambda_* \mathcal{H}_*}\right)^2 \ln^2\!\left[1 + \frac{\lambda_* \mathcal{H}_*}{2\pi s_{\rm turb}}\right], \tag{16}$$

which asymptotically tends to 1 for $\lambda_* \mathcal{H}_* \ll 2\pi s_{\rm turb}$. Since $s_{\rm turb} \gtrsim 1$ and $\lambda_* \mathcal{H}_* \leq 1$, one can compute the value of $S_{\rm turb}(s_{\rm turb})$ at $\lambda_* \mathcal{H}_* = 1$, to get $S_{\rm turb}(s_{\rm turb}) \gtrsim S_{\rm turb}(1) \simeq 0.86$. As $\lambda_* \mathcal{H}_*$ decreases, $S_{\rm turb}(1)$ quickly tends to 1, with a relative error below 1.6% when $\lambda_* \mathcal{H}_* < 0.1$. Hence, the assumption that $S_{\rm turb}$ is one at the frequency peak is accurate for most relevant cases.

The anisotropic stresses power spectrum, $p_\Pi(s_1)$, depends on the power spectrum of the kinetic turbulence and/or of the magnetic field. Here we assume that they follow the von Kármán spectral shape[2] (von Kármán 1948),

characterized by a Batchelor spectrum f^4 at low f, expected from causality (Durrer & Caprini 2003), and a turbulent Kolmogorov $f^{-5/3}$ spectrum at large f. Within this assumption, the normalized (i.e., $p_\Pi(0) = 1$) anisotropic stress power spectrum can be approximated as

$$p_\Pi(s_1) \simeq \left[1 + \left(\frac{s_1}{s_\Pi}\right)^{\alpha_\Pi}\right]^{-\frac{11}{3\alpha_\Pi}}, \tag{17}$$

where $\alpha_\Pi \simeq 2.15$ and $s_\Pi = 2.2$. Compared to the numerical computations in Roper Pol et al. (2022a) and Auclair et al. (2022), the maximum relative error of the analytical fit of Eq. (17) is below 6% for all frequencies $s_1 \leq 10$. At larger s_1, the relative error of the fit increases. However, since $p_\Pi \sim s_1^{-11/3}$, at higher frequencies $p_\Pi(s_1)$ has decayed below $\mathcal{O}(10^{-3})$.

Having normalized both $S_{\rm turb}$ and p_Π, the GW efficiency from (M)HD turbulence, $\mathcal{A}$ in Eq. (9), becomes [3] (Roper Pol et al. 2022a)

$$\mathcal{A} = \frac{112}{15}\sqrt{\frac{3}{5\pi^5}} \frac{\Gamma\!\left[\frac{13}{6}\right]\Gamma^2\!\left[\frac{17}{6}\right]}{\Gamma\!\left[\frac{17}{3}\right]\Gamma^2\!\left[\frac{1}{3}\right]} s_{\rm turb}\, p_\Pi(s_{\rm turb})$$
$$\simeq 2 \times 10^{-3} s_{\rm turb}\, p_\Pi(s_{\rm turb}), \tag{18}$$

where $s_{\rm turb}$, the peak frequency of the GW spectrum, is located where $s_1\, p_\Pi(s_1)$ is maximum:

$$s_{\rm turb} = \lambda_* f_{\rm turb} = s_\Pi \left(\frac{3}{8}\right)^{\frac{1}{\alpha_\Pi}} \simeq 1.4, \tag{19}$$

$$p_\Pi(s_{\rm turb}) = \left(\frac{11}{8}\right)^{-\frac{11}{3\alpha_\Pi}} \simeq 0.6. \tag{20}$$

Substituting these values into Eq. (18), the GW efficiency becomes

$$\mathcal{A} \simeq 1.75 \times 10^{-3}. \tag{21}$$

3. The SGWB and the magnetic field, relics of a first order phase transition

In this section we investigate which regions in the parameter space of a first order phase transition would lead to a SGWB detectable with LISA. We also compute the strength and correlation scale of the corresponding magnetic field, which would result from the amplification of a seed field by the MHD turbulence in the aftermath of the phase transition. We are ultimately interested in assessing whether a first-order phase transition could produce a SGWB detectable with LISA and, at the same time, an IGMF consistent with existing observational bounds. We therefore perform a systematic scan over the first-order phase transition parameter space. The SGWB is considered "detectable" by LISA if its spectrum exceeds the power law sensitivity (PLS) of LISA with a signal-to-noise ratio threshold of SNR = 10 (Caprini et al. 2020) at any frequency 10^{-5} Hz $< f < 0.1$ Hz. An illustrative example of the SGWB spectrum from turbulence and sound waves with LISA's sensitivity for the parameters choice $T_* = 100$ GeV, $\alpha = 0.5$, $\beta = 10H_*$, $v_w = 0.95$, and $\varepsilon_{\rm turb} = 1$ is shown in Fig. 1.

---

[2] The von Kármán spectrum can be expressed using, for example, Eq. (6) in Roper Pol et al. (2022a) with $\alpha = 6/17$.

[3] Note that Roper Pol et al. (2022a) uses a different notation, where $s_{\rm turb} \equiv k_{\rm GW}/k_*$, and our parameter $\mathcal{A}$ corresponds to $s_{\rm turb}\, p_\Pi(s_{\rm turb})\, \mathcal{C}/(8\pi^2 \mathcal{A}^2)$ in their Eq. (24).
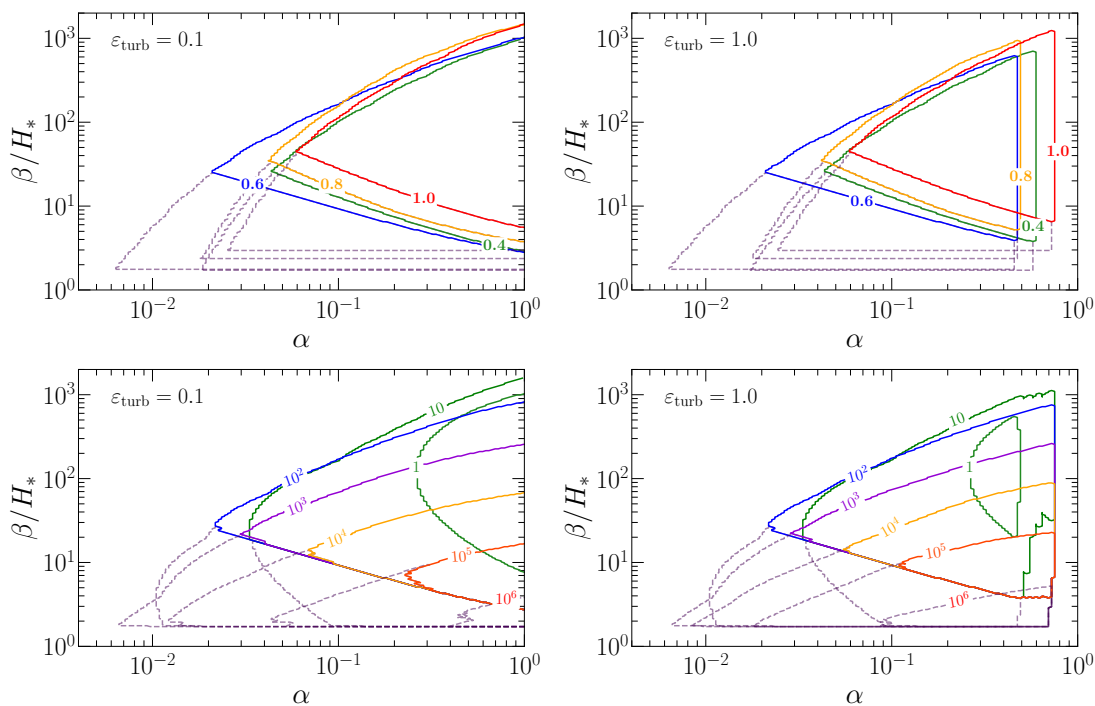
Fig. 2. Sensitivity reach of LISA in terms of the parameters α and β/H_* for different wall velocities v_w, combining all temperature scales (top panels), and for different temperatures T_* in GeV, combining all wall velocities (bottom panels), for $\varepsilon_{\rm turb} = 0.1$ (left) and 1 (right). The results shown correspond to the sound wave template based on the fit from the Higgsless simulations (c.f. Sec. 2.1). Coloured contours correspond to regions of the parameter space where $H_*\tau_{\rm nl} \lesssim 1$, while their continuation by dashed contours correspond to regions where $H_*\tau_{\rm nl} \gtrsim 1$.

We perform the analysis for two values of $\varepsilon_{\rm turb}$, the parameter characterising the relative amount of kinetic energy in (M)HD turbulence (see Eq. (10)): $\varepsilon_{\rm turb} = 0.1$ and 1. The ranges of the phase transition parameters are defined as follows. The broken-phase bubble wall speed is in the range $0.3 \leq v_w \leq 1$, where the lower limit ensures that $\lambda_* > \delta\lambda_*$, and the hierarchy of the breaks in the SSM SGWB spectral shape follows, as described in Sec. 2. The upper limits on α are computed such that the ratio of magnetic to total energy density, Ω_{B*}, does not exceed 10%, as imposed by BBN (Shvartsman 1969; Kahniashvili et al. 2011; Kawasaki & Kusakabe 2012).[4] The lower limits on β/H_* are set such that the resulting length scale is causal $\lambda_*\mathcal{H}_* \lesssim 1$. Furthermore, T_*, α, and β/H_* satisfy 1 GeV $\lesssim T_* \lesssim 3 \times 10^6$ GeV, $\alpha \gtrsim 5 \times 10^{-3}$, and $\beta/H_* \lesssim 2 \times 10^3$, as inferred by the results of the analysis of the detectability of the SGWB signal.

For each point in the 4-dimensional parameter space, we have reconstructed the SGWB signal and compared with LISA's sensitivity. Figure 2 shows the detectable regions in the $(\alpha, \beta/H_*)$ plane in two ways: *i)* for different wall velocities v_w, by combining the results for all temperatures T_* in the detectable range (upper panels), and *ii)* for different temperatures (in GeV) by combining the results for all v_w (bottom panels). The results shown in Fig. 2 are derived using the HL fit for the sound waves template of Eq. (7), since using the SSM template, given in Eq. (6), does not

lead to any appreciable difference when we compute the resulting magnetic field parameters.

It is usually argued (see, e.g., Caprini et al. (2020)) that turbulence is not produced if the time scale to develop non-linearities from sound waves is larger than one Hubble time, $H_*\tau_{\rm nl} \sim H_*\lambda_*/\sqrt{K} \gtrsim 1$. According to this criterion, we show in Fig. 2 the contours of the regions where turbulence is expected to develop by coloured lines, while the dashed lines correspond to the contours of the regions in the parameter space that would be, in principle, excluded by this condition.

Plasma motion induced by the first-order phase transition can excite (M)HD turbulence, which could amplify any pre-existing seed magnetic fields, for example generated via charge separation at the bubble walls (Sigl et al. 1997). Turbulence is expected to drive the magnetic field energy density to equipartition with the plasma kinetic energy density (Banerjee & Jedamzik 2004; Durrer & Neronov 2013). The equipartition argument suggests that the initial magnetic field configuration at the end of the phase transition is $B_* \simeq \sqrt{2\,\Omega_{B*}\,\rho_{\rm rad}^*} \simeq \sqrt{\Omega_*\rho_{\rm rad}^*}$ (see Eq. (11)), where we assume that the total energy density is $\rho_{\rm vac} + \rho_{\rm rad}^* \simeq \rho_{\rm rad}^*$ for weak and moderately strong phase transitions. After fixing the value of $\varepsilon_{\rm turb}$, using Eqs. (5) and (10) we can relate the magnetic field strength B_* at the phase transition time, assuming that both the turbulence generation and the establishment of equipartion are instantaneous, to the fraction of vacuum energy that is converted to kinetic energy κ_v, and ultimately to α using the prescription of Espinosa et al. (2010). Furthermore, the initial magnetic field correlation length would correspond to the characteristic fluid

---

[4] Relaxing the BBN limit has been recently proposed in Kahniashvili et al. (2022) by taking into account the turbulence decay from the magnetic field generation scale to BBN. However, we still restrict Ω_{B*} in our analysis to avoid relativistic Alfvén and velocity speeds, regime in which the SGWB templates have not been validated.
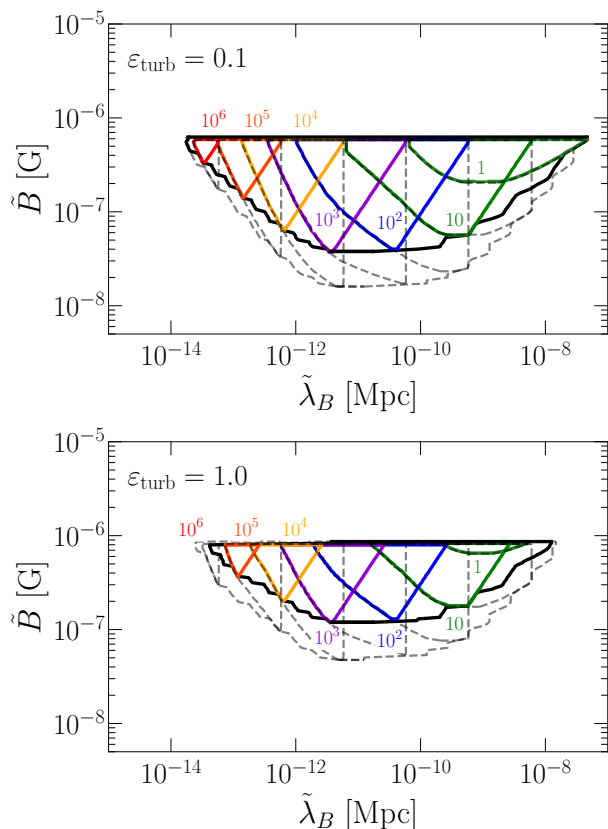
Fig. 3. Range of the comoving magnetic field strength $\tilde{B}$ and correlation length $\tilde{\lambda}_B$ corresponding to the contours in the lower panels of Fig. 2, for $\varepsilon_{\mathrm{turb}} = 0.1$ (top panel) and 1 (bottom panel).

scale λ_*, which is related to v_w, $c_s = 1/\sqrt{3}$, and β/H_* via Eq. (1).

Therefore, for each combination of the phase transition parameters analyzed above, we can infer the magnetic field parameters B_* and λ_*. As explained in Sec. 4, it is meaningful to express B_* and λ_* in terms of comoving quantities, $\tilde{B}$ and $\tilde{\lambda}_B$, as these are the initial conditions for the magnetic field evolution, i.e., the starting points in the magnetic field evolutionary paths. In Figure 3, we therefore show the ranges of the magnetic field parameters $\tilde{B}$ and $\tilde{\lambda}_B$ that correspond to the ranges of the phase transition parameters given in the bottom panels of Fig. 2, i.e., for different values of T_*. Since $K < 1$ and due to equipartition, the values of Ω_{B*} are limited to $0.5\,\varepsilon_{\mathrm{turb}}$. In addition, we have limited its value to a 10% of the total energy density because of the BBN bound and the condition of non-relativistic turbulence. Therefore, in this analysis $\Omega_{B*} \leq \min(0.1, 0.5\,\varepsilon_{\mathrm{turb}})$.

It appears from Fig. 3 that a phase transitions with parameters providing a SGWB accessible to LISA, and $\varepsilon_{\mathrm{turb}} = 1$ (upper panel), can lead to fairly strong magnetic fields with strengths up to $\tilde{B} \sim 10^{-6}$ G, corresponding to the limit $\Omega_{B*} \sim 0.1$. For $\varepsilon_{\mathrm{turb}} = 0.1$ (bottom panel), the upper limit $\Omega_{B*} \sim 0.05$ yields instead a maximal field strength of $\tilde{B} \sim 6 \times 10^{-7}$ G. The initial correlation length of the field can vary over a wide range, between 10^{-14} Mpc and 10^{-7} Mpc, depending on the temperature of the phase transition T_*, on its duration β^{-1}, and on the bubble wall velocity v_w. The region of parameter space where $H_*\tau_{\mathrm{nl}} \gtrsim 1$, indicated in Fig. 2 by the dashed contours at small α and

β/H_*, corresponds in Fig. 3 to the region where $\tilde{B}$ is small. As in Fig. 2, the contours in Fig. 3 correspond to the sound wave template based on the fit from the Higgsless simulations (c.f. Sec. 2.1); using the SSM template would not lead to any appreciable difference in the magnetic field parameters.

4. The magnetic field evolution and the IGMF today

After its generation at the phase transition, the magnetic field evolves following the laws of turbulent decay up to the recombination epoch; see, e.g., Durrer & Neronov (2013). Depending on the initial strength B_*, initial correlation length λ_*, and initial fractional helicity h, different turbulent evolutionary paths will lead to different IGMF today. In figure 4 we report, as initial conditions for the turbulent evolution, the regions in the parameter space given by the comoving initial strength $\tilde{B}$ and correlation length $\tilde{\lambda}_B$ that are compatible with a SGWB detectable by LISA according to the analysis presented in Sec. 3 (Figs. 2 and 3). Since the resulting SGWB signal is expected to depend very weakly on the fractional helicity (Roper Pol et al. 2022b), the initial condition regions are considered to be valid both for non-helical and helical magnetic fields. The black- and grey-shaded areas correspond to $\varepsilon_{\mathrm{turb}} = 1$ and 0.1, respectively. The orange-shaded region corresponds to what found in Roper Pol et al. (2022a), where the limiting case in which no sound waves are formed and all the kinetic energy from the plasma motion is in the form of MHD turbulence was analyzed. It is clear that including the sound waves contribution to the SGWB spectrum enlarges the range of magnetic field parameters compatible with a detectable GW signal.

Examples of possible evolutionary paths for helical and non-helical fields are also shown in Fig. 4 by inclined lines starting at the boundaries of the initial condition regions, with arrows pointing at the parameter values expected to be reached at recombination. The evolutionary paths depend on the magnetic field helicity. Helical magnetic fields with maximal helicity $h = 1$ are expected to follow the evolutionary path with $\tilde{B} \propto \tilde{\lambda}_B^{-1/2}$ in the $(\tilde{B}, \tilde{\lambda}_B)$ parameter space, due to helicity conservation (Banerjee & Jedamzik 2004; Durrer & Neronov 2013) (see purple dash-dotted lines in Fig. 4). The decay laws of non-helical fields are not completely understood. The hypothesis of "selective decay" of short-range modes would lead to the decay law $\tilde{B} \propto \tilde{\lambda}_B^{-5/2}$, while the hypothesis of conservation of the Hosking invariant (Hosking & Schekochihin 2022; Zhou et al. 2022) suggests the decay law $\tilde{B} \propto \tilde{\lambda}_B^{-5/4}$ (respectively dashed and solid green lines in Fig. 4).

The endpoint of the evolution is also uncertain, depending on whether the evolution time scale is determined by the Alfvénic (Banerjee & Jedamzik 2004) or the reconnection speed (Hosking & Schekochihin 2022). A straightforward estimate of the largest processed eddies at recombination suggests that the modes with $\tilde{\lambda} \lesssim v_A t_{\mathrm{rec}}$ are processed by turbulence (Banerjee & Jedamzik 2004), with v_A being the Alfvén velocity, defined in Eq. (11), and t_{rec} the Hubble time at recombination. In this case, setting $\tilde{\lambda}_B \equiv v_A t_{\mathrm{rec}}$, the final strength and correlation length satisfy the rela-
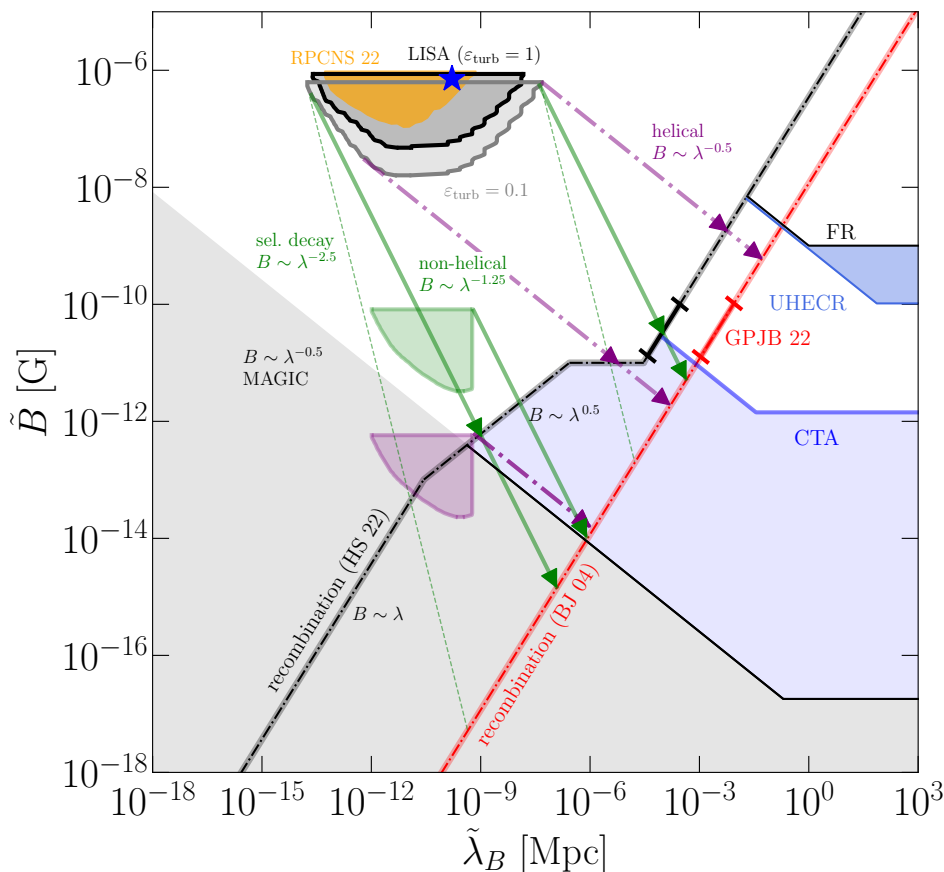
Fig. 4. Expected initial and final comoving strength and correlation length of a cosmological magnetic field generated at a first order phase transition with parameters leading to a SWGB detectable by LISA. The black and grey contours in the upper left corner of the figure show the parameter space of initial conditions if one assumes that, respectively, the totality ($\varepsilon_{\rm turb} = 1$) and 10% ($\varepsilon_{\rm turb} = 0.1$) of the sound wave kinetic energy is transferred to MHD turbulence. The orange-shaded region is the one found in Roper Pol et al. (2022a) (RPCNS 22) assuming that the SGWB is sourced exclusively by MHD turbulence. The blue star corresponds to the phase transition parameters for which the SGWB spectrum is shown in Fig. 1, considered for illustrative purposes. The inclined arrows show the envelopes of the evolutionary tracks. The dash-dotted purple arrows apply to helical fields, $B \sim \lambda^{-0.5}$, as given in Banerjee & Jedamzik (2004); the solid green arrows apply to non-helical fields, $B \sim \lambda^{-1.25}$, as given in Hosking & Schekochihin (2022); the dashed green arrows correspond to the hypothesis of "selective decay" of short-range modes for non-helical fields, $B \sim \lambda^{-2.5}$ (Banerjee & Jedamzik 2004). The black and red dash-dotted lines show the possible endpoints of the magnetic field evolution, corresponding to the IGMF present in the voids today, assuming respectively that the reconnection time scale dominates the magnetic field dynamics (Hosking & Schekochihin 2022) (HS 22) and that the Alfvénic time scale dominates the magnetic field dynamics (Banerjee & Jedamzik 2004) (BJ 04). The grey-shaded region at the bottom of the plot is excluded by the lower bound on the IGMF established by the MAGIC γ-ray observatory (Acciari et al. 2023). The dark blue and black thin lines show the upper limit on the IGMF from, respectively, ultra high energy cosmic rays (Neronov et al. 2021) and Faraday Rotation measures (Pshirkov et al. 2016). The blue-shaded area shows the range of IGMF parameters that will be probed by the γ-ray observatory CTA (Korochkin et al. 2021). The red and black ticks over the BJ 04 and HS 22 recombination lines correspond to the range of magnetic field strengths obtained in Galli et al. (2022), which would induce enough baryon clumping to help alleviating the Hubble tension, as proposed in Jedamzik & Pogosian (2020). The green and purple areas denote, respectively, the range of non-helical and helical magnetic field parameters that would arise from a first order phase transition occurring at $T_* \sim 100$ GeV and sourcing a SGWB detectable by LISA, fixing the smallest possible value $\varepsilon_{\rm turb}$ while still satisfying the MAGIC's lower bound. The values of $\varepsilon_{\rm turb}$ are $\mathcal{O}(10^{-9})$ (non-helical) and $\mathcal{O}(10^{-13})$ (helical).

tion Durrer & Neronov (2013)

$$\tilde{B} \simeq 10^{-8} \left[\frac{\tilde{\lambda}_B}{1\ \rm Mpc} \right]\ \rm G, \tag{22}$$

shown by the thick dash-dotted red line in Fig. 4. On the other hand, the evolution model put forward in Hosking & Schekochihin (2022) proposes that the relevant time scale for the turbulent evolution is the one determined by reconnection, and that the decay law for non-helical fields is governed by the conservation of the Hosking integral, related to local fluctuations of helicity. Within this model, the

correlation length at recombination can be smaller than the estimate in Eq. (22) by a factor of 20 for magnetic fields with final strength higher than 10^{-11} G; and even smaller for weaker fields — as much as by a factor of $10^{5.5}$ when the field strength is below 10^{-13} G (Hosking & Schekochihin 2022). The possible endpoints of the reconnection-driven evolution are represented by the thick dash-dotted black line in Fig. 4.

Figure 4 shows that the strength and correlation length of the IGMF resulting from the initial conditions leading to a SGWB detectable by LISA vary over a wide range:

10^{-9} Mpc $< \tilde{\lambda}_B < 10^{-1}$ Mpc and 10^{-17} G $< B < 10^{-9}$ G, depending on the fractional helicity h, on the uncertainty about the evolutionary path of non-helical fields, and on the uncertainty about the locus of the evolutionary endpoints.

It is also interesting to note that the phase transition parameters $(\alpha, \beta, v_w, T_*, \varepsilon_{\mathrm{turb}})$ providing a detectable SGWB correspond to a relic IGMF that could be probed either with γ-ray observations, or through its imprint on recombination. Given the uncertainty of the magnetic field helicity $0 < h < 1$, none of the $(\alpha, \beta, v_w, T_*, \varepsilon_{\mathrm{turb}})$ combinations detectable by LISA is currently ruled out by known upper bounds on the magnetic field inferred from the CMB (Ade et al. 2016), Faraday Rotation (FR) measures (Pshirkov et al. 2016), or ultra-high energy cosmic rays (UHECR) (Neronov et al. 2021). It has been proposed that primordial magnetic fields would also affect the CMB anisotropies through the production of small-scale baryonic density fluctuations (Jedamzik & Saveliev 2019). This leads to a stringent upper limit on the magnetic field amplitude, shown by the upper ticks on the red and black solid lines in Fig. 4 (Jedamzik & Saveliev 2019; Galli et al. 2022). According to this upper limit, a small range of the parameters detectable by LISA (i.e., large B_* and λ_* or, equivalently, large α, small β/H_*, and small T_*) would be ruled out, if the magnetic field is helical.

Remarkably, within the evolution model of Hosking & Schekochihin (2022), all initial conditions corresponding to a detectable SGWB would also result in an IGMF consistent with the lower bounds from the MAGIC γ-ray observations (Neronov & Vovk 2010; Acciari et al. 2023). Moreover, if the magnetic field is non-helical, the resulting field strength and correlation length would be within the sensitivity reach of the next-generation γ-ray observatory CTA (Korochkin et al. 2021), again for all initial conditions compatible with a detectable SGWB. Only a present-day IGMF with strength $\tilde{B} \gtrsim 10^{-11}$ G may not be accessible to CTA: this would correspond to most of the initial conditions parameter space, if the magnetic field is helical. However, in this case, the field should have left an observable imprint at recombination, detectable in the CMB (Jedamzik & Saveliev 2019; Galli et al. 2022). In any case, within the evolution model of Hosking & Schekochihin (2022), first-order phase transitions providing a detectable SGWB would have a complementary "multi-messenger" signature, either in the γ-ray or in the CMB data, even if the fraction of kinetic energy transferred to MHD turbulence is minimal.

This does not occur, instead, within the evolution model of Banerjee & Jedamzik (2004). This model proposes that the Alfvén speed determines the relevant time scale for the turbulent evolution, and that non-helical fields decay following the hypothesis of "selective decay" of short-range modes. Following this evolution, a non-helical magnetic field could have a present-day strength that is below the γ-ray lower bound. In this case, γ-ray observations would not rule out the corresponding $(\alpha, \beta, v_w, T_*, \varepsilon_{\mathrm{turb}})$ combination; they just imply that the observed IGMF must have been produced by a different process, and the field generated by the phase transition is not detectable on top of the dominant IGMF.

The range of IGMF parameters corresponding to a field strength at recombination that could help alleviating the Hubble tension via baryon clumping (Jedamzik & Pogosian 2020; Galli et al. 2022), is particularly interesting. It is indicated by the label GPJB 22 and the red interval in Fig. 4,

if one assumes that the Alfvénic speed determines the final values at recombination (Banerjee & Jedamzik 2004); and by the black interval if one considers the relevant time scale to be that of reconnection (Hosking & Schekochihin 2022). We find that, for *almost any* beyond-Standard-Model scenario resulting in a first-order phase transition that produces a SGWB detectable by LISA, there exists some fractional helicity h for which the magnetic field generated at the phase transition evolves into a sufficient strength at recombination to induce sufficient baryon clumping and help alleviating the Hubble tension. In this case, by combining a possible estimation of the magnetic field at recombination inferred from CMB data, with the other possible estimation inferred from the detection of a SGWB with LISA, one could fix the start and end points of the evolutionary path of the magnetic field and, in this way, provide a measurement of the initial helicity of the field.

At last, note that the transfer from the sound waves kinetic energy to MHD turbulence does not need to be very efficient in order to guarantee the "multi-messenger" signature. If the magnetic field produced at the phase transition is subdominant, i.e., $\varepsilon_{\mathrm{turb}} \ll 1$, then the SGWB would simply be dominated by the sound waves contribution, and it would still be detectable for appreciable ranges of the phase transition parameters $(\alpha, \beta, v_w, T_*)$. Correspondingly, even if $\varepsilon_{\mathrm{turb}} \ll 1$, there can still exist regions in the magnetic field parameter space that are compatible with the lower bounds from γ-ray observations. Fixing $T_* = 100$ GeV, we find that this happens provided $\varepsilon_{\mathrm{turb}} \gtrsim \mathcal{O}(10^{-13})$ for non-helical magnetic fields, and $\varepsilon_{\mathrm{turb}} \gtrsim \mathcal{O}(10^{-9})$ for helical fields. These initial conditions are shown respectively by the green and purple regions in Fig. 4.

5. Conclusions

We have analyzed the possibility of obtaining a "multi-messenger" signature of a cosmological first-order phase transition, if it leads to both a stochastic gravitational wave background detectable by LISA, and the generation of a primordial magnetic field that: *i)* leaves an imprint at recombination observable in the CMB data, and *ii)* populates the voids of the Large Scale Structure at present time with a strong enough intergalactic magnetic field to satisfy the lower bounds from γ-ray observations. This "multi-messenger" signature could be present even if a tiny fraction of the sound waves kinetic energy is transferred to MHD turbulence.

Adopting a phenomenological description of the phase transition in terms of five parameters $(\alpha, \beta, v_w, T_*, \varepsilon_{\mathrm{turb}})$, we have found the ranges of these parameters for which the gravitational wave background is within LISA's sensitivity reach (Fig. 2). For each of such parameter combinations, we have estimated the initial strength and correlation length of the primordial magnetic field that could be generated at the phase transition (Fig. 3). From these initial conditions, we have traced the field evolution in time until the present-day Universe, depending on the initial fractional helicity of the field (Fig. 4). To do so, we have adopted two possible evolution scenarios, put forward in Banerjee & Jedamzik (2004) and in Hosking & Schekochihin (2022). We find that in the latter case, all first-order phase transition parameter combinations that provide a gravitational wave backgorund detectable by LISA result in a magnetic field that would be detectable either via γ-ray observations, e.g., with the CTA

telescope, or through its imprint on the CMB. If the cosmological evolution of the magnetic field follows the model of Banerjee & Jedamzik (2004), it may happen that the magnetic field resulting from the phase transition is too weak to explain the intergalactic magnetic field.

References

Acciari, V. A. et al. 2023, Astron. Astrophys., 670, A145
Ade, P. A. R. et al. 2016, Astron. Astrophys., 594, A19
Afzal, A. et al. 2023, Astrophys. J. Lett., 951, L11
Agazie, G. et al. 2023, Astrophys. J. Lett., 951 [arXiv:2306.16213]
Amaro-Seoane, P. et al. 2017 [arXiv:1702.00786]
Antoniadis, J. et al. 2023a [arXiv:2306.16214]
Antoniadis, J. et al. 2023b [arXiv:2306.16227]
Auclair, P., Caprini, C., Cutting, D., et al. 2022, JCAP, 09, 029
Banerjee, R. & Jedamzik, K. 2004, Phys. Rev. D, 70, 123003
Bodeker, D. & Moore, G. D. 2017, JCAP, 05, 025
Brandenburg, A., Clarke, E., He, Y., & Kahniashvili, T. 2021, Phys. Rev. D, 104, 043513
Brandenburg, A., Enqvist, K., & Olesen, P. 1996, Phys. Rev. D, 54, 1291
Brandenburg, A., Kahniashvili, T., & Tevzadze, A. G. 2015, Phys. Rev. Lett., 114, 075001
Cai, R.-G., Wang, S.-J., & Yuwen, Z.-Y. 2023 [arXiv:2305.00074]
Caprini, C. & Figueroa, D. G. 2018, Class. Quant. Grav., 35, 163001
Caprini, C. et al. 2016, JCAP, 04, 001
Caprini, C. et al. 2020, JCAP, 03, 024
Dolag, K., Kachelriess, M., Ostapchenko, S., & Tomàs, R. 2011, ApJ, 727, L4
Durrer, R. & Caprini, C. 2003, JCAP, 11, 010
Durrer, R. & Neronov, A. 2013, Astron. Astrophys. Rev., 21, 62
Ellis, J., Lewicki, M., & No, J. M. 2020, JCAP, 07, 050
Espinosa, J. R., Konstandin, T., No, J. M., & Servant, G. 2010, JCAP, 06, 028
Galli, S., Pogosian, L., Jedamzik, K., & Balkenhol, L. 2022, Phys. Rev. D, 105, 023513
Gowling, C. & Hindmarsh, M. 2021, JCAP, 10, 039
Hindmarsh, M. 2018, Phys. Rev. Lett., 120, 071301
Hindmarsh, M. & Hijazi, M. 2019, JCAP, 12, 062
Hindmarsh, M., Huber, S. J., Rummukainen, K., & Weir, D. J. 2014, Phys. Rev. Lett., 112, 041301
Hindmarsh, M., Huber, S. J., Rummukainen, K., & Weir, D. J. 2017, Phys. Rev. D, 96, 103520, [Erratum: Phys.Rev.D 101, 089902 (2020)]
Hindmarsh, M. B., Lüben, M., Lumma, J., & Pauly, M. 2021, SciPost Phys. Lect. Notes, 24, 1
Hosking, D. N. & Schekochihin, A. A. 2022 [arXiv:2203.03573]
Jedamzik, K. & Pogosian, L. 2020, Phys. Rev. Lett., 125, 181302
Jedamzik, K. & Saveliev, A. 2019, Phys. Rev. Lett., 123, 021301
Jinno, R., Konstandin, T., Rubira, H., & Stomberg, I. 2023, JCAP, 02, 011
Kahniashvili, T., Clarke, E., Stepp, J., & Brandenburg, A. 2022, Phys. Rev. Lett., 128, 221301
Kahniashvili, T., Tevzadze, A. G., & Ratra, B. 2011, Astrophys. J., 726, 78
Kajantie, K., Laine, M., Rummukainen, K., & Shaposhnikov, M. E. 1996, Nucl. Phys. B, 466, 189
Kamionkowski, M., Kosowsky, A., & Turner, M. S. 1994, Phys. Rev. D, 49, 2837
Kawasaki, M. & Kusakabe, M. 2012, Phys. Rev. D, 86, 063003
Korochkin, A., Kalashev, O., Neronov, A., & Semikoz, D. 2021, Astrophys. J., 906, 116
Neronov, A., Semikoz, D., & Kalashev, O. 2021 [arXiv:2112.08202]
Neronov, A. & Vovk, I. 2010, Science, 328, 73
Pshirkov, M. S., Tinyakov, P. G., & Urban, F. R. 2016, Phys. Rev. Lett., 116, 191302
Reardon, D. J. et al. 2023, Astrophys. J. Lett., 951 [arXiv:2306.16215]
Roper Pol, A., Caprini, C., Neronov, A., & Semikoz, D. 2022a, Phys. Rev. D, 105, 123502
Roper Pol, A., Mandal, S., Brandenburg, A., & Kahniashvili, T. 2022b, JCAP, 04, 019
Roper Pol, A., Mandal, S., Brandenburg, A., Kahniashvili, T., & Kosowsky, A. 2020, Phys. Rev. D, 102, 083512
Shvartsman, V. F. 1969, Pisma Zh. Eksp. Teor. Fiz., 9, 315
Sigl, G., Olinto, A. V., & Jedamzik, K. 1997, Phys. Rev. D, 55, 4582
Stephanov, M. A. 2006, PoS, LAT2006, 024
Subramanian, K. 2016, Rept. Prog. Phys., 79, 076901
Vachaspati, T. 2021, Rept. Prog. Phys., 84, 074901
von Kármán, T. 1948, Proceedings of the National Academy of Sciences, 34, 530
Xu, H. et al. 2023 [arXiv:2306.16216]
Zhou, H., Sharma, R., & Brandenburg, A. 2022, J. Plasma Phys., 88, 905880602